Transition of Near-Ground Vorticity Dynamics during Tornadogenesis

JANNICK FISCHER[a] AND JOHANNES M. L. DAHL[a]

[a]*Department of Geosciences, Texas Tech University, Lubbock, Texas*

(Manuscript received 5 July 2021, in final form 9 November 2021)

ABSTRACT: Although much is known about the environmental conditions necessary for supercell tornadogenesis, the near-ground vorticity dynamics during the tornadogenesis process itself are still somewhat poorly understood. For instance, seemingly contradicting mechanisms responsible for large near-ground vertical vorticity can be found in the literature. Broadly, these mechanisms can be sorted into two classes, one being based on upward tilting of mainly baroclinically produced horizontal vorticity in descending air (here called the downdraft mechanism), while in the other the horizontal vorticity vector is abruptly tilted upward practically at the surface by a strong updraft gradient (referred to as the in-and-up mechanism). In this study, full-physics supercell simulations and highly idealized simulations show that both mechanisms play important roles during tornadogenesis. Pretornadic vertical vorticity maxima are generated via the downdraft mechanism, while the dynamics of a fully developed vortex are dominated by the in-and-up mechanism. Consequently, a transition between the two mechanisms occurs during tornadogenesis. This transition is a result of axisymmetrization of the pretornadic vortex patch and intensification via vertical stretching. These processes facilitate the development of the corner flow, which enables production of vertical vorticity by upward tilting of horizontal vorticity practically at the surface, i.e., the in-and-up mechanism. The transition of mechanisms found here suggests that early stages of tornado formation rely on the downdraft mechanism, which is often limited to a small vertical component of baroclinically generated vorticity. Subsequently, a larger supply of horizontal vorticity (produced baroclinically or via surface drag, or even imported from the environment) may be utilized, which marks a considerable change in the vortex dynamics.

KEYWORDS: Baroclinic flows; Tornadogenesis; Trajectories; Supercells; Tornadoes; Idealized models; Large eddy simulations; Tracers

1. Introduction

In an attempt to elucidate the dynamics of supercell tornadoes, several competing theories about how parcels of air may acquire large vertical vorticity near the surface have been discussed in the recent literature. Broadly, these theories fall into two classes, one of which requires the presence of a downdraft, while the other merely requires a strong horizontal updraft gradient to achieve rotation practically at the ground level.

The "downdraft mechanism" was first proposed by Davies-Jones (1982), although speculations about the role of downdrafts in tornadogenesis date back even further (e.g., Ludlam 1963). Davies-Jones argued that in an environment with large horizontal vorticity but devoid of vertical vorticity, an updraft alone cannot achieve large vertical vorticity at the surface via vortex-line reorientation. The reason is that as the horizontal vorticity is reoriented into the vertical within the updraft gradient, parcels are rising away from the ground. Even though vertical vorticity may arise via tilting during this process, the vertical vorticity does not become significant very near the surface and hence cannot explain the formation of tornadoes. An example of this scenario was analyzed by Davies-Jones and Markowski (2013), who considered tilting of near-surface horizontal vorticity along an intense gust front. They found that the horizontal vorticity is greatly diminished as parcels approach the gust front due to strong horizontal deceleration near the stagnation point. While there is a strong updraft gradient, the vorticity available to be tilted upward is vanishingly small. Above the surface, however, this mechanism does account for large vertical vorticity (e.g., Markowski et al. 2014). Many other studies have formally investigated the source mechanism for near-ground vertical vorticity maxima in full-physics simulations. These studies are summarized in Table 1. The downdraft mechanism was identified in numerical simulations of supercells by Davies-Jones and Brooks (1993), Markowski and Richardson (2014), Wicker and Wilhelmson (1995), Adlerman et al. (1999), Dahl et al. (2014), Schenkman et al. (2014), Dahl (2015), Parker and Dahl (2015), and Fischer and Dahl (2020), and a similar argument exists for quasi-linear convective system (QLCS) tornadoes (Trapp and Weisman 2003; Schenkman and Xue 2016; Flournoy and Coniglio 2019; Boyer and Dahl 2020). In most of these studies, the mechanism relies heavily on baroclinic production of horizontal vorticity at the periphery of a downdraft. This vorticity vector is then reoriented into the vertical while parcels descend toward the ground. The process as a whole is often referred to as the Davies-Jones and Brooks (1993) mechanism. Three aspects are noteworthy:

(i) In the analysis by Schenkman et al. (2014), the horizontal vorticity in descending air was not generated baroclinically, but via surface drag.
(ii) In the original Davies-Jones and Brooks (1993) picture, the horizontal, baroclinically produced vorticity was purely streamwise, while in many of the simulations above this vorticity has a substantial crosswise component (which becomes more streamwise as the parcel turns toward the incipient vortex after most of the baroclinic production is finished).

Corresponding author: Jannick Fischer, jannick.fischer@ttu.edu

DOI: 10.1175/JAS-D-21-0181.1

TABLE 1. A selection of studies that included an analysis of the sources for vertical vorticity or circulation near the lowest model level. The "mechanism" column was subjectively determined if the authors did not make an explicit statement pointing to one or the other mechanism. If an entry could not be determined with certainty from our subjective interpretation, it was filled with a long dash. For stretched or nested grids, Δx and Δz pertain to the respective central domain. Low-level mesocyclone is abbreviated as "ll-meso."

	Δx, Δz	Bottom boundary	Analysis target	Analysis type	Type of trajectory	Below z_1	Mechanism
Rotunno and Klemp (1985)	1 km, 500 m	Free-slip	ll-meso	Both	Backward	Yes	Downdraft
Davies-Jones and Brooks (1993)	1 km, 200 m	Free-slip	ll-meso	Parcels	Backward	Yes	Downdraft
Wicker and Wilhelmson (1995)	120 m, 120 m	Free-slip	TLV, ll-meso	Parcels	Backward	Yes	Both
Adlerman et al. (1999)	500 m, 100 m	Free-slip	ll-meso	Parcels	Forward	No	Both
Trapp and Weisman (2003)	1 km, 300 m	Free-slip	Mesovortex	Parcels	Backward	Yes	Downdraft
Mashiko et al. (2009)	50 m, 40 m	Semi-slip	TLV	Parcels	Backward	—	In-and-up
Markowski and Richardson (2014)	100 m, 100 m	Free-slip	TLV	Both	Forward	No	Both
Naylor and Gilmore (2014)	100 m, 100 m	Free-slip	Varying	Parcels	Backward	Yes	—
Dahl et al. (2014)	250 m, 100 m	Free-slip	ζ rivers	Parcels	Forward	No	Downdraft
Schenkman et al. (2014)	50 m, 20 m	Semi-slip	TLV	Parcels	Backward	Yes	In-and-up
Dahl (2015)	250 m, 100 m	Free-slip	ζ maxima	Parcels	Forward	No	Downdraft
Parker and Dahl (2015)	250 m, 100 m	Free-slip	ζ rivers	Parcels	Forward	No	Downdraft
Markowski (2016)	100 m, 20 m	Both	TLV	Circulation	Backward	Yes	Downdraft
Mashiko (2016)	50 m, 20 m	Semi-slip	TLV	Both	Backward	Yes	In-and-up
Roberts et al. (2016)	50 m, 20 m	Semi-slip	TLV	Parcels	Backward	No	In-and-up
Rotunno at al. (2017)	100 m, 2 m	Free-slip	TLV	Parcels	Forward	No	In-and-up[a]
Yokota at al. (2018)	50 m, 10 m	Semi-slip	TLV	Both	Backward	—	In-and-up
Flournoy and Coniglio (2019)	333 m, 25 m	Semi-slip	Mesovortex	Parcels	Forward	No	Both
Tao and Tamura (2020)	50 m, 10 m	Semi-slip	TLV	Both	Backward	Yes	In-and-up
Boyer and Dahl (2020)	200 m, 20 m	Free-slip	TLV	Parcels	Forward	No	In-and-up
Fischer and Dahl (2020)	100 m, 60 m	Free-slip	ζ patch	Parcels	Forward	No	Downdraft

[a] In their analysis, downdrafts were critical (because they provided large horizontal vorticity stretching), but not in the sense of the downdraft mechanism as defined in this study.

(iii) The ambient vorticity does not seem to contribute meaningfully to vertical vorticity production in this scenario (Dahl et al. 2014; Dahl 2015).

The second mechanism does not rely on downdrafts and has recently received more attention, perhaps starting with the Schenkman et al. (2014) study. Here, a parcel's large horizontal vorticity (in their analysis greatly augmented by surface drag) is tilted upward close to the ground rather than in descending air to produce large vertical vorticity practically at the surface. This mechanism has since been identified also by Mashiko (2016), Roberts et al. (2016), Yokota et al. (2018), Flournoy and Coniglio (2019), Tao and Tamura (2020), and Boyer and Dahl (2020). In fact, earlier studies such as those by Klemp and Rotunno (1983), Wicker and Wilhelmson (1993), Adlerman et al. (1999) and Mashiko et al. (2009) had already pointed to this mechanism. Likewise, in simulations of tornadoes (e.g., Lewellen and Lewellen 2007, their Fig. 6) and dust devils (Simpson and Glezer 2016, their Fig. 21), it is also implied (although not usually explicitly stated) that horizontal vorticity is tilted upward close to the surface where the initially horizontal inflow erupts upward forming the corner flow (e.g., Rotunno 2013) (this may be inferred by noticing that angular momentum contours correspond to vortex lines in the meridional plane in axisymmetric flows; e.g., Parker 2012). Rotunno et al. (2017) showed analytically that the upward tilting of horizontal vorticity near the surface may indeed lead to appreciable vertical vorticity practically at the surface. This horizontal vorticity may include the ambient vorticity (which is due to a combination of mesoscale and synoptic-scale processes, including surface drag), as well as storm-generated vorticity (notably generated baroclinically and also via surface drag). Hence, this mechanism has much more "access" to different vorticity sources as compared to the downdraft mechanism, which typically relies only on baroclinic vorticity. Throughout the rest of the paper, this second mechanism will be referred to as the "in-and-up" mechanism.[1] A small caveat with most of the above-cited studies is that the analyzed parcel trajectories tended to descend below the lowest scalar model level (see Table 1), which makes them susceptible to errors (e.g., Vande Guchte and Dahl 2018).

The conflict between the two mechanisms can perhaps be attributed to a lack of understanding of the tornadogenesis process itself. Through decades of research, a relatively robust understanding of tornadic storm environments (e.g., Rasmussen and Blanchard 1998; Parker 2014; Coniglio and Parker 2020) and supercell storm-scale dynamics (e.g., Rotunno 1981; Rotunno and Klemp 1982; Davies-Jones 1984; Rotunno and Klemp 1985; Davies-Jones 2002; Dahl 2017) has emerged. The dynamics of mature tornadoes has also been studied

[1] In-and-up here describes the fate of the horizontal vorticity vector, which reaches the vortex and is then abruptly tilted upward.

extensively, including, e.g., vortex breakdown, the exceedance of the thermodynamic speed limit, and small-scale structures such as those resulting from 3D instabilities (e.g., Fiedler and Rotunno 1986; Lewellen 1993; Nolan 2012; Dahl 2021). However, the interface between the storm-scale and tornado-scale dynamics and specifically the near-ground dynamics during tornadogenesis are still poorly understood. Traditionally, the final step of tornadogenesis has been described as contraction of the near-ground mesocyclone (e.g., Davies-Jones 2015). This picture is perhaps based on early Doppler radar observations and numerical simulations of tornadic supercells, which had relatively coarse spatial and temporal resolution [see, e.g., French et al. (2013), regarding the importance of high-resolution Doppler-radar observations]. More recent studies with increased resolution reveal a higher level of detail in the tornadogenesis process. For instance, simulations show multiple subtornadic vortices merging to form the final tornado (e.g., Orf et al. 2017), and Dahl (2020) demonstrated that the self-organization of sheet-like vortex patches near the surface is a necessary step in vortex genesis.

As it stands, there seems to be ample evidence that both mechanisms, the downdraft mechanism and the in-and-up mechanism, are relevant during the tornado life cycle (see Table 1). The question that remains is which of these mechanisms dominates in which situation. To tackle this problem, regions with relatively large vertical vorticity developing in the outflow region of different simulated supercells are analyzed with the aid of relatively long history trajectories. The focus lies on the relevance of the in-and-up and downdraft mechanisms at different stages of the tornado life cycle. The primary sources of vorticity are also discussed.

The remainder of the paper is structured into two main parts. In the next section we will present full-physics simulations in horizontally homogeneous supercell environments to provide a first comparison of the vorticity dynamics at different vortex stages. In section 3, a more idealized approach will be presented, in which the full evolution of an elliptical vortex patch into a tornado is analyzed in depth. The results are discussed in section 4 and a summary is offered in section 5.

2. Full-physics simulations

In this part of the study, two full-physics supercell simulations will be presented to analyze both the dynamics of a pretornadic vortex patch and of a mature tornado separately. Both simulations used the same homogeneous base state (as described next), but one used updraft nudging for storm initiation, while the other used a warm bubble. As discussed in section 2b, the nudging led to unrealistically large *initial* surface vorticity production in the outflow, which "kick-started" a strong and long-lived tornado-like vortex. In contrast, the gentler bubble simulation seemed more realistic, but did not produce a long-lived tornado-like vortex. Hence, the warm-bubble initialization was chosen to analyze a more realistic pretornadic vortex patch in section 2c, while the nudging technique was used to analyze the mature vortex in section 2d.

a. Model setup

The full-physics supercell simulations used the Bryan Cloud Model version 1 (CM1; Bryan and Fritsch 2002) release 19.7 and were based on Coffer and Parker (2017) with the following adaptations. A horizontal grid spacing of 200 m was used in the inner domain (100 km × 100 km), stretched to 1800 m toward the edges of the outer domain with 200 km × 200 km.[2] The vertical grid spacing was as in Coffer and Parker (2017) with 20 m in the lowest 300 m, stretched to 280 m at 12 km, and then remaining constant up to model top at 18.16 km. At this grid resolution, simulated vortices did not fully represent real tornadoes and were merely tornado-like vortices (TLVs). However, as will be shown, the resolution was high enough to demonstrate the different dynamics compared to pretornadic vortex patches. A higher resolution will be used to analyze the same difference of vorticity dynamics in more detail in the idealized part of this study (section 3), whose model setup will be introduced in section 3a.

All simulations used the near-inflow tornadic VORTEX2 composite sounding (Parker 2014) and a semi-slip bottom boundary condition with a drag coefficient of 0.0014, which, with the vertical grid described above, corresponds to a roughness length of $z_0 = 0.02$ cm. As in Coffer and Parker (2017), the Coriolis force only acted on the perturbation winds, which implies a balanced base-state wind profile. Usually, a spinup of the simulation is required to establish this force balance. However, since the resulting changes in the hodograph in Coffer and Parker (2017) were small, the spinup was neglected here. Recently, Davies-Jones (2021) also suggested that designing the base state with this method introduces an invented force and hence unphysical results. However, it is still unclear whether this impact is significant in environments such as the one used here, and the vorticity budgets presented in sections 2c and 2d do not exhibit obvious errors that might arise from the invented force.

Furthermore, random potential temperature perturbations of 0.25 K were added to the base state to encourage turbulent mixing (Markowski and Bryan 2016). Both a simulation with Morrison (section 2c) and one with NSSL microphysics (section 2d) will be presented.

b. A potential problem in simulations with strong updraft nudging

Initially following Coffer and Parker (2017), the storms were initiated with the updraft nudging technique proposed in Naylor and Gilmore (2012) [Coffer and Parker (2017), and many recent studies, employed relatively strong updraft nudging over 1200 s with $w_{max} = 15$ m s^{-1} and horizontal and vertical radii of 15 and 2.5 km]. The simulations using this technique reliably produced strong TLVs in outflow air between 45 and 80 min, consistent with Coffer and Parker (2017) and Coffer et al. (2017). In contrast, initiation with a warm bubble (with θ'_{max} between 3 and 6 K and similar dimensions as the updraft nudging) did not result in a strong TLV.[3]

[2] Control simulations with constant horizontal grid spacing did not meaningfully differ from the ones presented here.

[3] All simulations (with any strength of updraft nudging or warm bubble tested) featured a short-lived TLV before outflow was developed. This vortex is deemed somewhat unphysical (e.g., Markowski 2016) and was hence not considered here, similar to many recent studies (e.g., Coffer and Parker 2017).

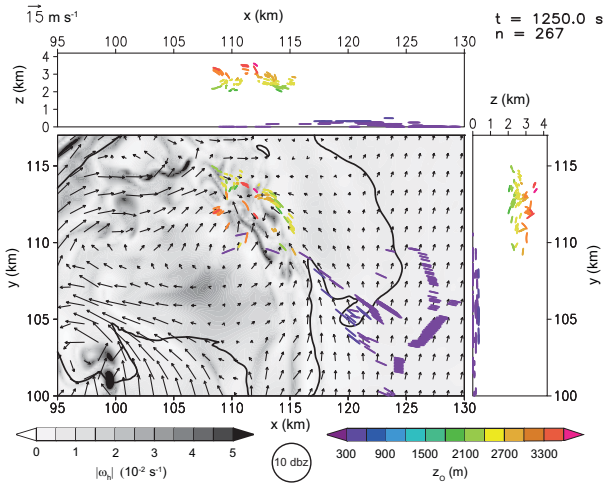

FIG. 1. A simulation with strong updraft nudging. Shown are the first 50 s (1200–1250-s model time) of 267 parcel trajectories that enter a near-ground vertical vorticity maximum at 2880 s, shortly before it develops into a TLV. Horizontal vorticity (shaded), horizontal wind vectors, and the 10-dBZ contour (black) are also shown at 2941 m AGL, which is approximately the mean origin height of the high-altitude parcels. The trajectory color indicates the origin height z_0.

To understand this systematic difference in tornado potential, trajectory analysis (the details of which are described in section 2c) was performed for parcels contributing to vertical vorticity maxima that subsequently developed into the strong TLV in a simulation with updraft nudging. A large subset of these parcels (Fig. 1) originated between 2 and 4 km above ground level (AGL), a relatively high altitude compared to other studies (e.g., Markowski et al. 2014; Dahl 2015). In these areas, the horizontal vorticity was artificially enhanced around the forced updraft (Figs. 1 and 2a). Some of this horizontal vorticity is realistic (baroclinic generation around the updraft), but the artificial forcing likely had some contribution. Furthermore, the initial downdraft pulse was relatively strong, possibly as a result of the large, forced mass flux in the nudged updraft. This facilitated parcels from this rather unusual source region to rapidly descend to the surface. With a warm bubble initiation, horizontal vorticity around the updraft was much weaker (Fig. 2b) and the downdraft developed more gradually. It seems that because of these differences, initial vertical vorticity maxima in the outflow were almost an order of magnitude weaker in the warm bubble simulation (Fig. 2d) compared to the simulation with updraft nudging (Fig. 2c) [this refers to the vertical vorticity maxima north of the updraft in the outflow. Directly below the updraft the simulations were still influenced by the early vortexgenesis (see footnote 3) and hence similar].

This characteristic of simulations with updraft nudging is consistent with the observation by Coffer and Parker (2018) that their simulated supercells developed "ample subtornadic surface vertical vorticity." A more thorough investigation of this issue is outside the scope of this paper, but might be important because the findings here suggest that the updraft nudging technique is not less unphysical than a warm bubble. In Fig. 1, a second group of parcels originated relatively close to the ground and from the inflow. However, since the high-altitude parcels already seemed unnatural, these near-ground parcels will not be discussed here further. For this study, we were not comfortable using simulations with updraft nudging to analyze the source mechanisms for *pretornadic* vertical vorticity in section 2c, and the warm bubble technique was used instead. However, to analyze the vorticity dynamics of a fully developed TLV in section 2d, a simulation with updraft nudging as in Coffer and Parker (2017) was used, following the argument that the dynamics of a *fully developed* TLV do not depend on how initial vorticity maxima were generated.

c. *Vorticity dynamics of pretornadic vortex patches*

After initiation of the storm with a 5 K thermal bubble (with horizontal and vertical radii of 10 and 1.4 km, respectively, centered at $x = 90$, $y = 90$, and $z = 1.4$ km), the updraft developed into a supercell with a hook-shaped reflectivity pattern (not shown). The first near-ground vorticity maxima in the outflow were weak (compared to simulations with updraft nudging) but slowly became more intense after the supercell structure became established toward the end of the first hour of the simulation (not shown). One of these vortex patches finally rolled up into a weak and short-lived TLV. The source mechanism for the initial vertical vorticity (ζ) of this patch will be analyzed in the following with the aid of forward trajectories.

First, an array of forward trajectories that initially covered the outflow and inflow over a 60 km × 60 km × 6 km grid was calculated between 1800 and 3600 s to determine the source regions for parcels entering the vortex patch of interest. Then, a new, denser set of 5 400 000 forward trajectories that covered these source regions was launched at 1800 s. Figure 3a shows a subset of these parcels which later entered the selected vortex patch[4] at 3600 s, prior to the intensification and roll-up into a rather symmetric TLV. These 126 trajectories are consistent with those identified numerous times before when pretornadic vorticity was investigated (e.g., Dahl 2015). All these parcels originated from east of the updraft. They then entered the forward flank region of the supercell, where they descended. The upper-level parcels descended much faster than the ones at low levels and, as a result, the parcels converged in the same area while making a left turn toward the updraft. An average parcel was calculated after filtering out 35 of the 126 parcels which descended below the lowest scalar model level (Vande Guchte and Dahl 2018) and 16 parcels which had an average difference between the integrated (as described below) and modeled ζ greater than 0.005 s^{-1}. For

[4] Between 3590 and 3610 s, the selected parcels had to reach $\zeta > 0.005\ s^{-1}$ while being in a box around the vortex patch between 10 and 50 m AGL.

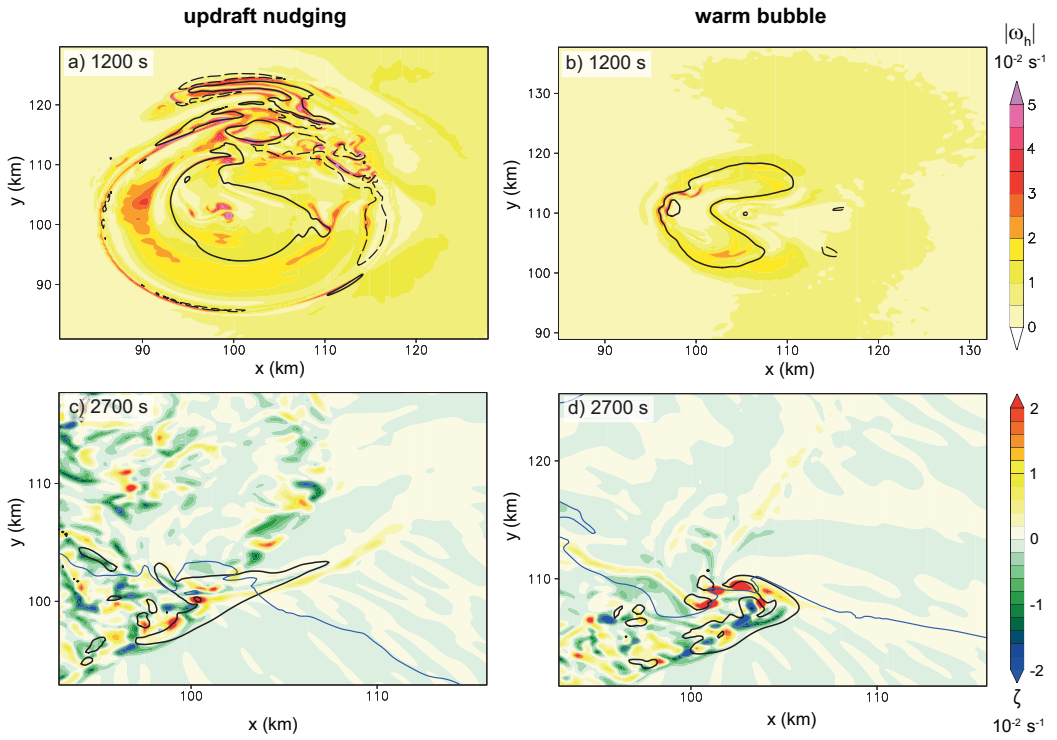

FIG. 2. (a),(b) Horizontal vorticity (shaded) and vertical velocity (+8 m s^{-1} solid black, −3 m s^{-1} dashed black) at 3.3 km AGL and 1200 s. (c),(d) Vertical vorticity at the lowest model level (shaded), 3 m s^{-1} vertical velocity (black), and 10-dBZ reflectivity (blue) contoured at 490 m AGL, both at 2700 s. (left) The simulation initiated with strong updraft nudging and (right) the one with the 6-K warm bubble.

the remaining 75 parcels, the fate of the vorticity vector was determined by integrating the 3D vorticity equation (e.g., Boyer and Dahl 2020)

$$\frac{d\boldsymbol{\omega}}{dt} = \underbrace{(\boldsymbol{\omega}\cdot\nabla)\mathbf{v} - \boldsymbol{\omega}(\nabla\cdot\mathbf{v})}_{\text{tilting/stretching}} + \underbrace{\frac{1}{\rho^2}\nabla\rho\times\nabla p}_{\text{baroclinic generation}} + \underbrace{\nabla\times\mathbf{F}}_{\text{diffusion/SGS mixing}}, \tag{1}$$

where $\boldsymbol{\omega}$ is the vorticity vector, $\mathbf{v}$ the velocity vector, ρ the density, p the pressure, and the vector $\mathbf{F}$ describes diffusion and subgrid-scale (SGS) mixing. Effects from surface friction were captured in the SGS mixing (turbulence) term by specifying the SGS stress at the lower boundary using the semi-slip bottom boundary condition (e.g., Markowski and Bryan 2016). Averaging these integrated forcing terms (with 5-s output intervals) over all parcels yielded the average vorticity budgets shown in Figs. 3b,c. The integrated vorticities (sum of the individual forcing terms; dashed red lines in Figs. 3b,c) match the interpolated values from the model grid (solid red lines) relatively well.

On average, horizontal vorticity production (Fig. 3b) was dominated by the baroclinic term during descent. This horizontal vorticity had both crosswise and streamwise components (not shown). Subsequent intensification of horizontal vorticity was due to horizontal tilting as the trajectories took the left turn, and due to stretching while the parcels diverged as they left the downdraft. After the parcels reached the lowest altitude (nadir) around 3500 s, horizontal vorticity decreased in the area of horizontal convergence below the updraft.

The vertical vorticity (Fig. 3c) was near zero before the parcels entered the forward flank. Then, as the parcels descended, downward tilting of horizontal vorticity produced negative ζ. Some of this negative ζ was reduced due to horizontal divergence, as shown in the stretching term. Subsequently, once the tilting term increased again during the last 600 s of the average parcel's descent, *the tilting resulted in positive ζ 400 s before the parcel reached the nadir. This means these parcels fall into the "downdraft mechanism" category*. Specifically, they are consistent with the classic baroclinic downdraft mechanism (Davies-Jones and Brooks 1993).

d. Vorticity dynamics of developed TLVs

As discussed in section 2b, the updraft nudging technique (with w_{max} = 15 m s^{-1}, horizontal and vertical radii of 15 and 2.5 km and centered at x = 100, y = 100, and z = 2.5 km; ramped down to zero between 1000 and 1200 s) was used to produce a simulation with a strong TLV. The simulation evolved similarly to the tornadic VORTEX2 composite simulations by Coffer and Parker (2017) and Coffer et al. (2017). An early, unphysical tornadic phase (see, e.g., Markowski 2016) was followed by a long-lived TLV in outflow air between 45 and 85 min. This latter vortex formed below the main updraft of the supercell and then intensified. In the following, this most intense tornadic period will be analyzed. As in the previous section, the analysis

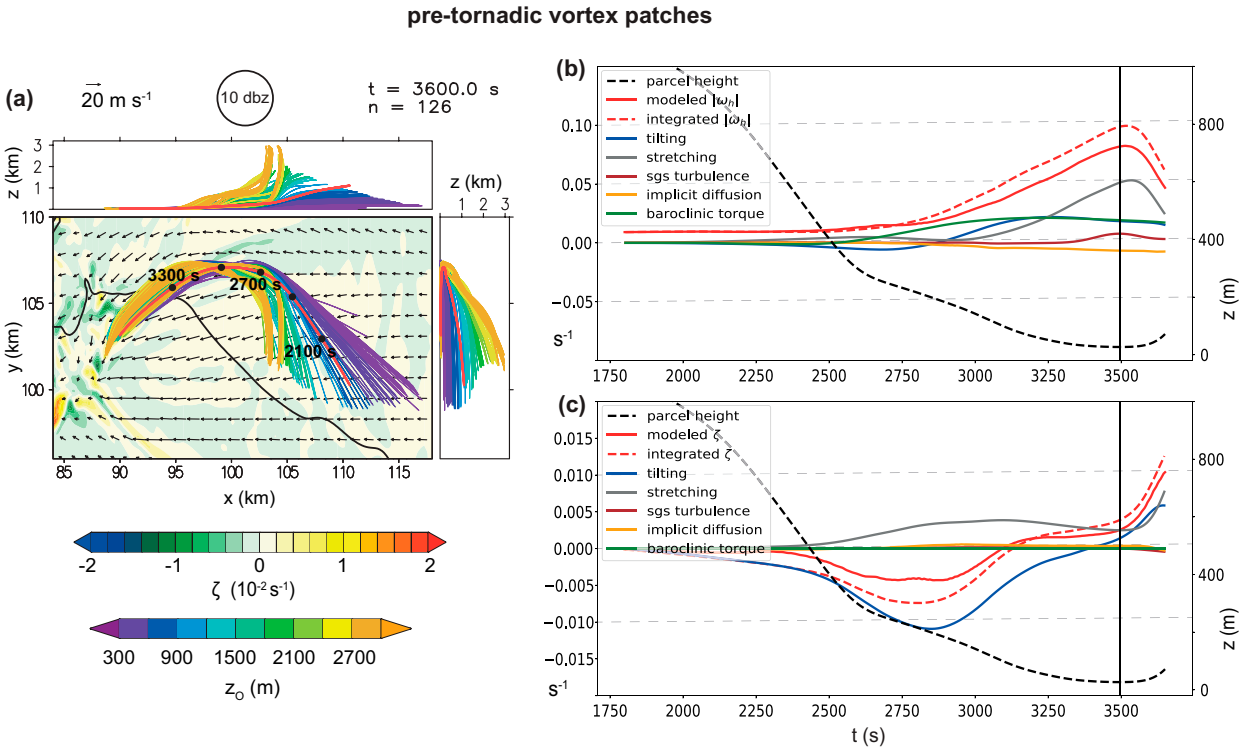

FIG. 3. Parcel analysis for the pretornadic vortex patch discussed in the text. (a) The 126 forward trajectories entering the vortex patch are color coded for their origin height z_0. Black points along the average parcel trajectory (red) show model time in 300-s increments. Vertical vorticity at 10 m AGL is shaded. (b) Horizontal vorticity and (c) vertical vorticity budget of the average parcel. The individual integrated terms of the vorticity equation are colored following the legend. Parcel height in dashed black follows the secondary y axis. The time when the parcel reached the nadir is indicated with a vertical black line.

was focused on how parcels acquired ζ. This was done using the same forward trajectory approach as in section 2c by releasing parcels at 2400 s, almost 30 min before the time of interest. Figure 4a shows the 184 parcels that entered the TLV and acquired $\zeta > 0.1\ \text{s}^{-1}$ between 4120 and 4170 s while being between 10 and 50 m AGL. In contrast to the parcels found in section 2c, numerous trajectories without a history of descent were found here, in addition to the parcels that descended in the forward flank region.

Unfortunately, the integrated vorticity budgets showed that most parcels (from the inflow and outflow) were highly influenced by implicit diffusion, especially in proximity of the tornado. It does not seem that these parcels dynamically contribute to the vortex, but rather gain their ζ via diffusion of vorticity that has been generated by other processes. In addition, the complex flow near the TLV in combination with the fact that parcels entered the TLV at different time steps, greatly smoothed any average budgets that were computed. For these reasons, a representative parcel for which diffusive effects were not dominant will be presented here instead of an average parcel.[5] Figure 4a shows the trajectory of this representative parcel and Figs. 4b–d the corresponding vorticity budgets for the final 300 s before the parcel entered the TLV.

The parcel descended in the forward flank region and then turned left toward the updraft before entering the tornadic circulation. The parcel's ζ was close to zero as the parcel ended the descent and approached the vortex around 4130 s (Figs. 4c,d). Subsequently, ζ increased abruptly close to the nadir via tilting of horizontal vorticity and then intensified via vertical stretching in the TLV. The horizontal vorticity available for tilting was mainly increased via surface drag, tilting, and stretching during the final 100 s of the approach. To assess the robustness of these results, the average ζ over all of the parcels that stayed above the lowest scalar model level (n = 81) was added to Fig. 4d (the average was taken after syncing the parcels relative to the time that they reached the nadir; see Fischer and Dahl 2020). The short decrease or "dip" in the average ζ upstream of the nadir in Fig. 4d was mainly due to implicit diffusion and is commonly observed in simulations (e.g., Schenkman et al. 2014; Markowski et al. 2014; Boyer and Dahl 2020). The subsequent increase of ζ was also dominated by the implicit diffusion term in many parcels (not shown). Nevertheless, almost all of these parcels had zero or negative ζ shortly before reaching the nadir, which means they behaved similarly to the reference parcel in the way that they all developed ζ abruptly via upward tilting and stretching while entering the TLV.

[5] The budgets of all 184 parcels were compared manually to make sure the chosen parcel was representative for the majority of parcels, disregarding parcels for which the implicit diffusion term was the main contributor to horizontal or vertical vorticity.

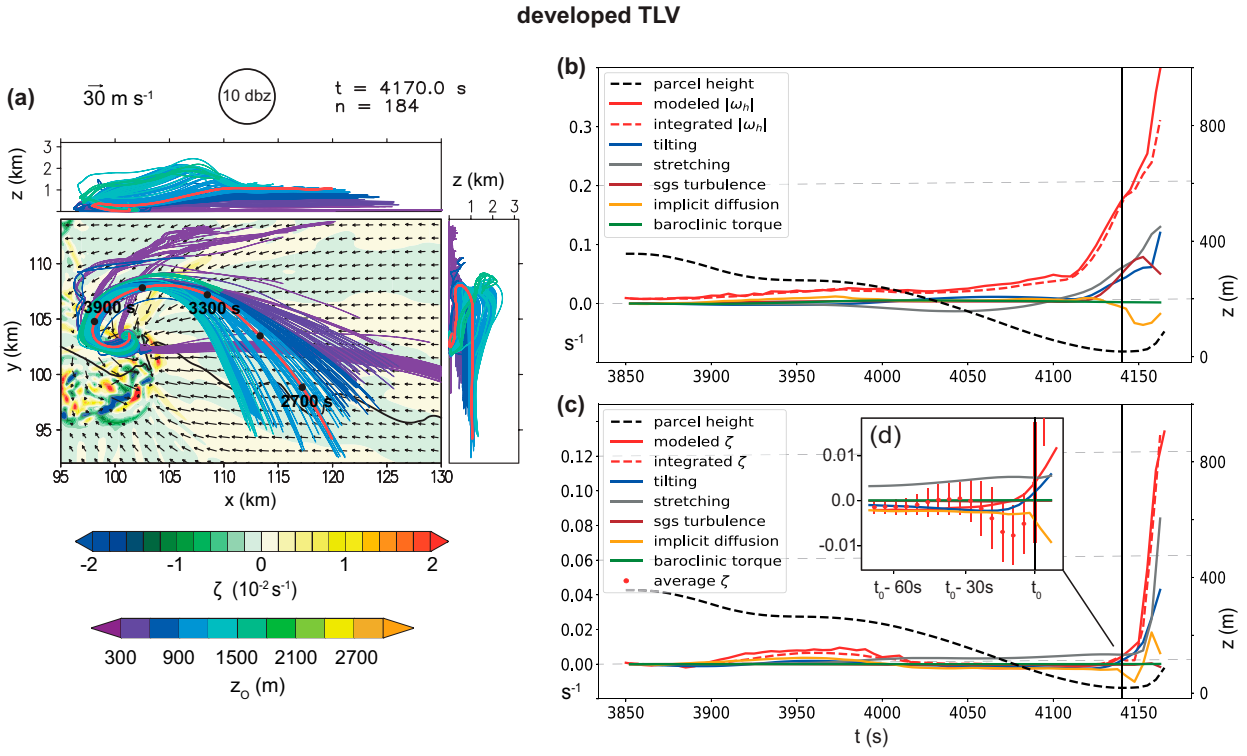

FIG. 4. As in Fig. 3, but for 184 parcels entering a developed TLV. (b)–(d) The vorticity budgets are for one representative parcel (see text). In (d), a zoomed-in view of the time period when the parcel entered the vortex was added. The red points represent the modeled vertical vorticity averaged over all selected parcels (see text) and the error bars show one standard deviation around this average. The time on the abscissa is relative to the time t_0 when the parcels reached the nadir (z = 18.2 m).

Overall, these results suggest that, in contrast to pretornadic vortex patches as in 2c, *the in-and-up mechanism is dominant at the mature tornado stage*, consistent with, e.g., Lewellen and Lewellen (2007). The picture emerges that during tornadogenesis the near-ground vorticity dynamics transitions from the downdraft mechanism to the in-and-up mechanism. To support this idea, a more idealized approach will be presented next.

3. Idealized simulations of tornadogenesis

So far, it has been shown that the pre-TLV vortex patch is maintained by the downdraft mechanism and that a mature TLV is maintained mainly by the in-and-up mechanism. In this section, we seek to further analyze the hypothesized transition from the downdraft to the in-and-up mechanism by considering the evolution of an idealized vortex patch.

a. Idealized model setup

For the simulations presented in this section, CM1 version 19.7 was used in a dry configuration. The Coriolis parameter was zero. The 10 km × 10 km inner domain had a horizontal grid spacing of 50 m, which has been found small enough to reproduce the general tornado structure in recent studies (e.g., Roberts et al. 2020). Outside this inner domain, the grid spacing was gradually increased to 550 m toward the domain boundary. The total domain size measured 40 km × 40 km. In the lowest 500 m, the vertical grid spacing was 10 m, which gradually increased to 190 m at 5500 m (model top). As described below, an artificial heat source was used to produce a strong low-level updraft, and subsequently an elliptical vortex patch was artificially introduced in the lowest 400 m. This setup combines the recent idealized approaches of Dahl (2020) and Fischer and Dahl (2020).

The two most commonly used bottom boundary conditions for storm-scale modeling (free-slip and semi-slip) both have disadvantages with respect to realistically representing the influence of surface friction on the flow. The free-slip condition ignores the negative surface momentum flux that is surface drag, which is known to influence the flow in tornadoes (e.g., Davies-Jones 2015). The semi-slip condition implements surface drag by parameterizing the SGS stress at the bottom boundary, but it is unclear how realistic the underlying assumptions are for thunderstorm in- and outflow (Markowski et al. 2019; Davies-Jones 2021) and the vertical wind shear is often overestimated (Markowski and Bryan 2016). For these reasons, two simulations (one free-slip and one semi-slip) will be presented to cover a range of possible behaviors for the available treatments of the lower boundary. In the latter, a drag coefficient C_D = 0.002 was used, yielding z_0 = 0.06 cm, a similar roughness length as in section 2. Larger values of C_D impacted the structure of the simulated tornadoes, but the general results remained the same.

The wind relative to the fixed heat source was set to a fixed velocity, which was realized by setting the base-state wind to zero but using an eastward-moving domain with $u_0 = 3$ m s^{-1}. This nonzero motion was added to aid the advection of the vortex patch below the updraft. Furthermore, this meant that the surface drag resulting from the semi-slip bottom boundary condition only acted on the perturbation winds. The largest horizontal velocity perturbations were produced by convergence below the updraft or around the vortex patch, and exceeded 3 m s^{-1} in these areas. This resulted in significant amounts of horizontal vorticity in the lowest model levels in the semi-slip run while the horizontal vorticity was close to zero everywhere near the ground in the free-slip run. The base-state potential temperature profile was similar to that used by Fischer and Dahl (2020) with $\theta = 300$ K at the lowest scalar model level (5 m AGL), increasing with 0.001 K km^{-1} up to 5 km AGL, and with 0.015 K km^{-1} above 5 km. This upper layer served to avoid undesirable interactions of the updraft with the model top. Furthermore, Rayleigh damping was applied above 5 km AGL. Since a turbulent inflow has been deemed important for realistic near-ground vortex structure (Bryan et al. 2017), random temperature perturbations of up to 0.25 K were added to introduce turbulence to the flow.[6]

As in Fischer and Dahl (2020), the model top (5.5 km) was much lower than in typical supercell simulations, because instead of modeling the whole storm, the strong low-level updraft was directly created in the model using a cylindrical heat source. The heat source center was placed at $x = -1000$, $y = 0$, and $z = 700$ m and had a horizontal radius of 2000 m and a total depth of 500 m. The heat source magnitude was held constant throughout the simulations with $S_{w0} = 0.08$ K s^{-1} [see Markowski and Richardson (2014) and Fischer and Dahl (2020) for a detailed description]. In contrast to Fischer and Dahl (2020) and Markowski and Richardson (2014), the updraft was nonrotating because no shear was present in the base-state flow.[7]

To mimic the behavior of the downdraft mechanism that delivers surface ζ to the updraft, we followed Dahl (2020) and prescribed an elliptical, cyclonic vortex patch with a depth of 400 m, which was placed upstream of the heat source (Figs. 5a,b). This vortex patch approach can be seen as an alternative to traditional idealized simulations, which often use a rotating domain to introduce global angular momentum which gets contracted to a tornado along the central axis by an overlying buoyancy source (e.g., Fiedler 1993; Parker 2012; Bryan et al. 2017). In the authors' view, the vortex patch method is more suitable for specifically studying the vortex-scale dynamics during tornadogenesis. Since it was desired that the updraft was fully developed before releasing the vortex patch, this patch could not be introduced at model start time. Instead, the vertical vorticity in the region of the patch was gradually added via the momentum tendency equations in CM1 over a time period of 10 s, starting at 320 s. The result was that ζ increased by 0.003 s^{-1} over 10 s, leading to $\zeta_{max} = 0.03$ s^{-1} at the center of the ellipse at 330 s (Figs. 5a,b). Since advection with the ambient flow and diffusion did not have a significant effect during the 10-s ramp-up time, the ellipse maintained its shape over this period. The initial placement of the ellipse was at $x = 300$ m, $y = 100$ m. The vertical vorticity within the patch decreased linearly from the center to the sides of the ellipse, with a length of the minor axis of 1 km and a length of the major axis of 4 km. The major axis was placed perpendicularly to the inflow east of the updraft (Figs. 5a,b) to allow for a relatively symmetric evolution. Other orientations of the patch relative to the updraft were also tested, often resulting in a less symmetric vortex patch roll-up but with essentially the same outcome. Furthermore, ζ was left constant with height between 0 and 100 m AGL to avoid artificial generation of horizontal vorticity in that layer. Between 100 and 400 m AGL, ζ decreased linearly to a value of zero.

In summary, two simulations with free-slip and semi-slip bottom boundary conditions and otherwise identical model configurations were performed. A heat source produced a nonrotating updraft, which was fully developed by around 330 s. Then, an elliptic vortex patch with a depth of 400 m was added upstream of the updraft.

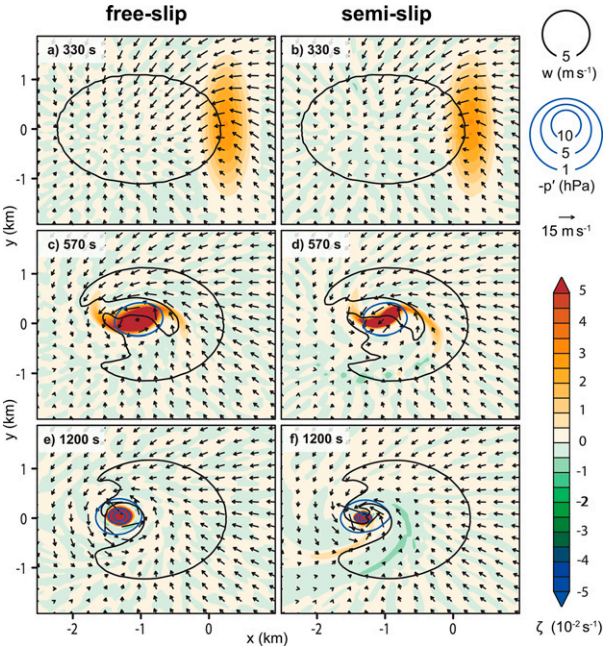

FIG. 5. Evolution of the idealized simulations. (a),(c),(e) Free-slip simulation at 330, 570, and 1200 s, respectively, and (b),(d),(f) semi-slip simulation at the same times. Vertical vorticity at the lowest scalar model level (5 m AGL) is shaded, pressure perturbation at the same level is in blue contours, and vertical velocity at 725 m AGL is in black contours. Every fifth wind vector in x and y is also shown at 5 m AGL.

[6] Sensitivity tests showed that the general results did not change in simulations without added turbulence.

[7] In the semi-slip run, horizontal vorticity associated with surface drag and differential acceleration into the low-level updraft led to a weak couplet of ζ at midlevels. However, the couplet remained at the edges of the updraft and the associated dynamic pressure perturbations were negligible.

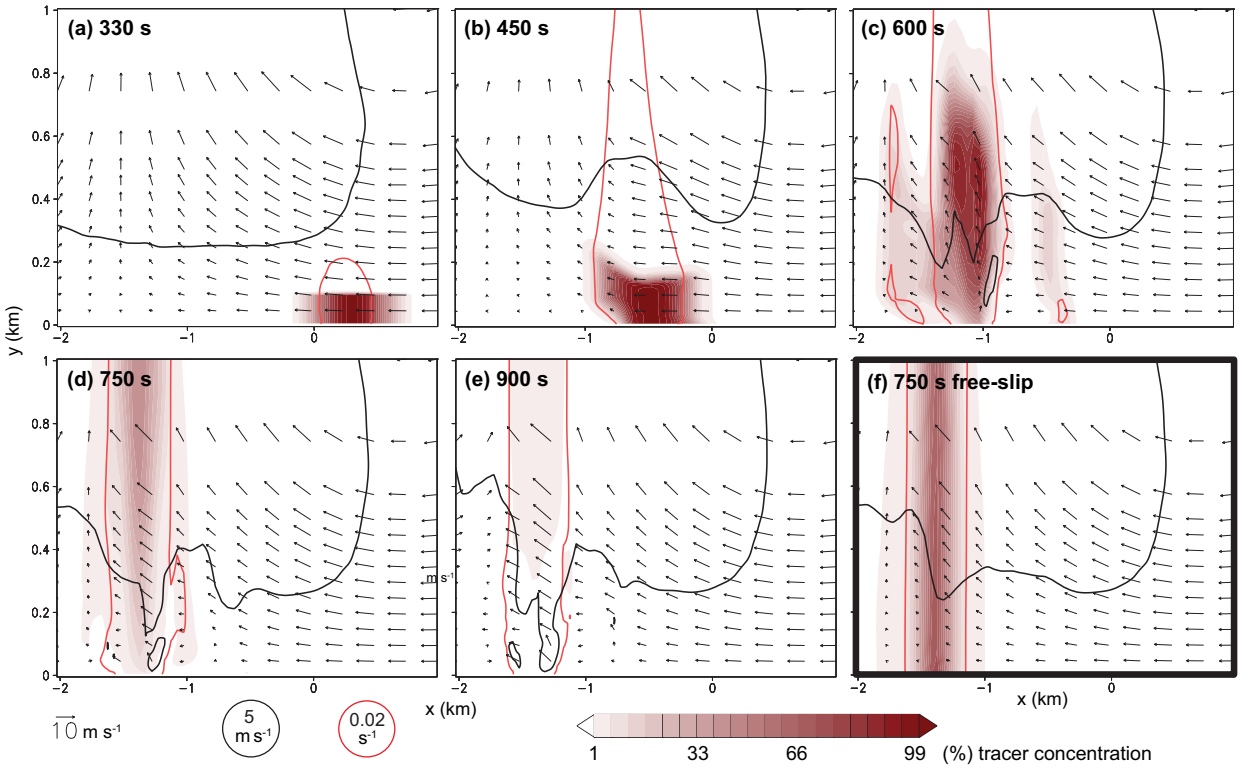

FIG. 6. Vertical cross sections (in the x–z plane) at different times during the roll-up and intensification of the vortex patch. (a)–(e) Semi-slip run from 330 to 900 s and (f) free-slip run at 750 s. Passive tracer concentration (in percentage of the initial concentration in the center of the ellipse) is shaded for tracers that were released in the lowest 100 m of the vortex patch at 330 s. The 3 m s^{-1} vertical velocity contour (black), the 0.02 s^{-1} vertical vorticity contour (red), and every fifth wind vector in the x–z plane are also shown. The cross sections were taken at y = 100 m, approximately through the center of the developing vortex.

b. *Evolution of the vortex patch into a tornado*

Figures 5a and 5b show the free-slip and the semi-slip simulations at 330 s, just after the elliptical vortex patch was added upstream of the updraft. In the subsequent time period, the vortex patch rolled up into an almost symmetric vortex [similar to the 2D simulations in Dahl (2020)] while it was advected westward below the updraft (Figs. 5c,d). Meanwhile vertical-vorticity-rich air from the upper portions of the vortex patch was advected upward into the updraft. This implies a vertical extension of the vortex into the updraft and hence vortex stretching. As a result, the vertical vorticity and horizontal wind speed increased while the pressure in the core decreased by several hPa (Figs. 5c–f). Finally, at around 1200 s (Figs. 5e,f) the vortices reached a relatively steady state, in which they persisted for the rest of the simulations (until 1800 s).

The roll-up of the vortex patches in the two simulations was generally similar to one another. However, some important differences were apparent and had a significant impact on the vorticity dynamics. In the semi-slip run, the near-ground wind field prior to the release of the vortex patch was slightly different than in the free-slip simulation, which resulted in a less symmetric shape of the spiraling vortex patch (Figs. 5c,d). More importantly, the influence of surface drag slowed the perturbation wind near the ground, which resulted in the formation and intensification of a corner-like flow in the semi-slip run (e.g., Davies-Jones 2015). Figures 6a–e shows this intensification via the 3 m s^{-1} vertical velocity contour, which lowers to the ground between 600 and 900 s, and Fig. 7b shows the final two-celled vortex structure in more detail at 1200 s. At this fully developed stage, the maximum vertical velocity was greater than 10 m s^{-1} in the lowest 20 m in the annular corner region around an internal downdraft in the core. In contrast, the free-slip run developed almost no vertical motion in the lowest few hundred meters and was hence in near-cyclostrophic balance (Fig. 7a).

To illustrate the change in near-ground vortex structure, passive tracers were released in a restart run for both simulations at 330 s. The tracers were only added in the lowest 100 m of the vortex patch and with the highest concentration in the center, decreasing linearly to the lateral edges of the ellipse (Fig. 6a). In both the free-slip and the semi-slip simulations, the tracer concentration stayed high near the ground during the roll-up and stretching of the vortex patch (Fig. 6b) until around 600 s (Fig. 6c). However, with formation of the corner-like flow, the tracer concentration rapidly decreased in the semi-slip run because near-ground vortex patch air was completely evacuated upward into the vortex (Figs. 6d,e). This was not the case in the free-slip run, which developed almost no vertical motion near the surface

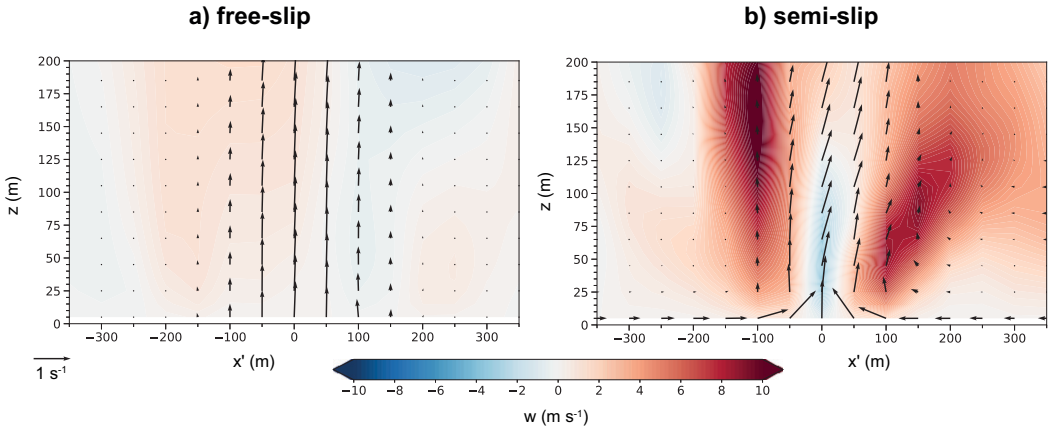

FIG. 7. Vertical cross sections through the developed vortices at 1200 s in (a) the free-slip and (b) the semi-slip simulations. Black vectors show vorticity in the x–z plane. Vertical velocity is shaded. The cross sections were taken along the x axis through the point of lowest pressure at the lowest model level. The x' axis is relative to this point.

(Fig. 6f). To investigate differences in the vorticity dynamics during this transition from an elliptical vortex patch to a tornado, two different time periods were compared and analyzed with separate sets of forward trajectories: the roll-up period before a rather symmetric vortex developed (section 3c) and the fully developed vortex (section 3d).

c. *Vorticity dynamics during vortex patch roll-up*

For the roll-up phase, t_1 = 570 was chosen as reference time[8] because this was roughly the time before the vortex became axisymmetric and developed an annular corner flow (Figs. 6c–e). An array of 1.2 million forward trajectories was launched at model start in a 10 km × 10 km grid around the center of the domain. Then we determined all parcels that were part of the developing vortex within 10 s before or after the reference time t_1 (only parcels with a minimum ζ of 0.1 s^{-1} and a height between 5 and 50 m were selected). Figure 8 shows the trajectories at an early time (330 s) when the ellipse was added to the flow and Figs. 9a and 9b show the same trajectories a few minutes later at the respective reference time t_1. In both simulations *all parcels that later made up the developing near-ground vortex were also part of the vortex patch* at 330 s. The fact that the near-ground parcels in the vortex were also part of the ellipse might appear trivial at first, but as will be shown in section 3d, it demonstrates a fundamentally different mechanism at work during the early stages than at later stages of the tornado.

In both simulations, the parcels artificially acquired ζ between 320 and 330 s when the vortex patch was added, thereby mimicking ζ that would come from the downdraft mechanism in real supercells (see section 2c). The artificial ζ acquisition can be seen in the vorticity budgets of the average parcels (Figs. 10b,d; see also Figs. 9a and 9b for the average parcel trajectories).[9] Since this source of ζ was artificially added to the momentum tendency (see section 3a), it was not part of the vorticity tendencies saved for the parcel budgets, resulting in a separation between the modeled and integrated ζ (red shading in Figs. 10b,d). However, after this ζ was added, the budget evolved naturally.

In the free-slip case, ζ was subsequently intensified purely by stretching while the parcel moved below the updraft embedded in the vortex patch (Fig. 10b). All other terms of the ζ budget were negligible. Note that neither the base-state wind profile nor the vortex patch contained horizontal vorticity in the lowest 100 m. Hence, the average parcel's horizontal vorticity was near zero (Fig. 10a), although individual parcels had some weak horizontal vorticity with random orientation due to the θ' added to the model (not shown).

In the semi-slip run, the average parcel acquired significant horizontal vorticity from surface drag (Fig. 10c), which was subsequently intensified via horizontal tilting and stretching during the roll-up of the vortex patch. Furthermore, as mentioned above, the roll-up in the semi-slip run was somewhat asymmetric. In contrast to the free-slip run, the asymmetry caused a small contribution to ζ through tilting of horizontal vorticity and implicit diffusion, as well as a growing error of the integrated compared to the modeled ζ (Fig. 10d). However, it is clear that stretching of the artificially generated ζ was the dominant process during the intensification phase in both simulations.

[8] Choosing a reference time 60 s earlier or later did not change the overall results.

[9] The average parcel for each run was calculated from the mean of the tendency terms of all individual parcels after filtering out 82 (74) parcels, which descended below the lowest scalar model level, and 30 (21) parcels for which $\overline{\left|\zeta_{\text{modeled}} - \zeta_{\text{integrated}}\right|} > 0.01\,\text{s}^{-1}$ in the free-slip (semi-slip) run. These criteria left 142 of 254 parcels in the free-slip and 35 of 130 parcels in the semi-slip case for calculation of the average parcel.

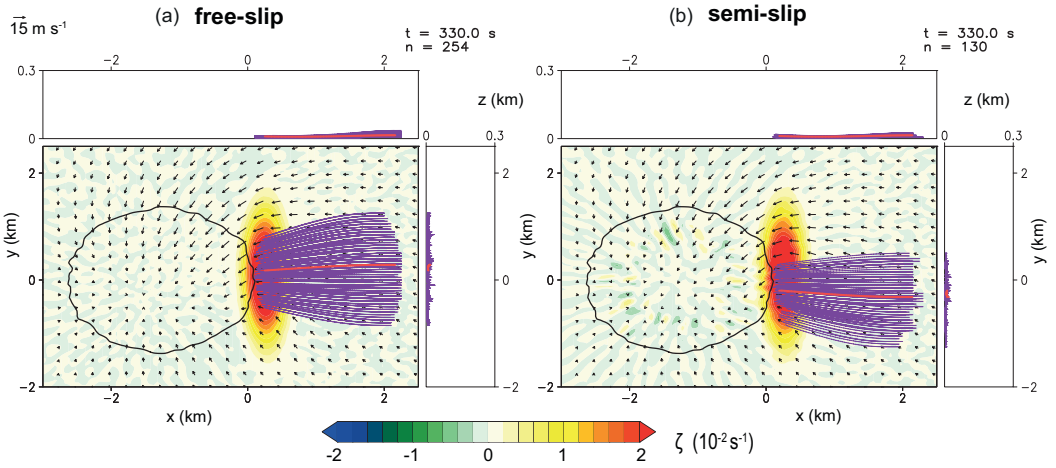

FIG. 8. Trajectories for the roll-up period at $t = 330$ s, the time when the elliptic vortex patch was added. The parcels are the same as shown in Figs. 9a and 9b. The near-ground vertical vorticity (shaded), the 5 m s^{-1} updraft contour at 725 m (black), and horizontal wind vectors were added as qualitative reference. The red parcels are the average parcels for which budgets were calculated in Fig. 10.

d. Vorticity dynamics of a developed vortex

For the mature vortex stage, the chosen reference time for both simulations was $t_2 = 1200$ s (Figs. 5e,f). The same analysis as in section 3c was performed for forward trajectories that were released at 600 s and entered the developed vortex at t_2. Focusing on the semi-slip run first, Fig. 9d shows that *these parcels did not have a single region of origin*. The trajectories spiraled in from all directions, except from the southeastern quadrant, which was blocked by a downdraft that formed south of the tornado, similar to an occlusion downdraft. The difference to the observed trajectories during the roll-up period is mainly due to the developing tornado structure and annular corner flow, which allows for new parcels to enter the tornado near the ground. Before analyzing this transition, it is noted that the free-slip run showed very different dynamics. As already suggested by the tracer concentrations (Fig. 6c), Fig. 9c shows that in contrast to the semi-slip run, almost no new parcels enter the developed vortex (a few trajectories originate from outside the vortex, but they acquire ζ solely from implicit diffusion and thus do not contribute dynamically to the vortex core). The reason is that with a free-slip bottom boundary, the vortex can be in cyclostrophic balance at the ground and parcels barely ascend as they spiral around the vortex center. This might be different in full-physics simulations, as will be discussed in section 4c. Since the free-slip simulation did not produce a realistic near-ground vortex structure, it is inappropriate to analyze the developed tornado stage here. Therefore, only the semi-slip run will be analyzed next.

New parcels entered the developed tornado after spiraling inward from multiple directions (Fig. 9d). Nevertheless, the vorticity dynamics were similar among all trajectories and will therefore be presented for an average parcel (red trajectory in Fig. 9d). Surface drag was the dominant source of initial horizontal vorticity production (Fig. 11a).[10] Large tilting and stretching further increased the amount of horizontal vorticity as the parcel got within a few hundred meters of the vortex, even though implicit diffusion and SGS mixing led to a reduction of horizontal vorticity.

The vertical vorticity remained near zero or was even slightly negative until the parcel reached the tornado (Figs. 11b,c). Then, ζ increased abruptly (within one to three integration steps of 5 s), mostly via tilting, and subsequently greatly intensified via stretching during rapid ascent in the vortex. Implicit diffusion tended to contribute to the generation of ζ as well, mostly because some parcels which contributed to the average were dominated by diffusive effects. However, the abrupt ascent and tilting of horizontal vorticity (generated by surface drag) into the vertical and subsequent stretching dominated the near-surface ζ generation at the developed vortex stage. This is consistent with the cross section in Fig. 7b, showing the vorticity vectors in the meridional plane. Horizontal vorticity was maximized in the lowest model levels, and rapid upward tilting and stretching of the vorticity vectors occurred below the vertical velocity maximum in the annular corner flow.

In conclusion, the idealized simulations are consistent with the full-physics simulations in section 2, showing a transition to the in-and-up mechanism during vortex intensification.

4. Discussion

a. Transition of the mechanisms

Both the full-physics and the idealized simulations in sections 2 and 3 of this study have demonstrated that the mechanisms leading to large near-ground vertical vorticity are different in the pretornadic and tornadic stages. The conclusion thus presents itself that a transition of the relevant mechanism leading to large near-surface vertical vorticity occurs during tornadogenesis. At first, the downdraft mechanism is the dominating contributor to significant but

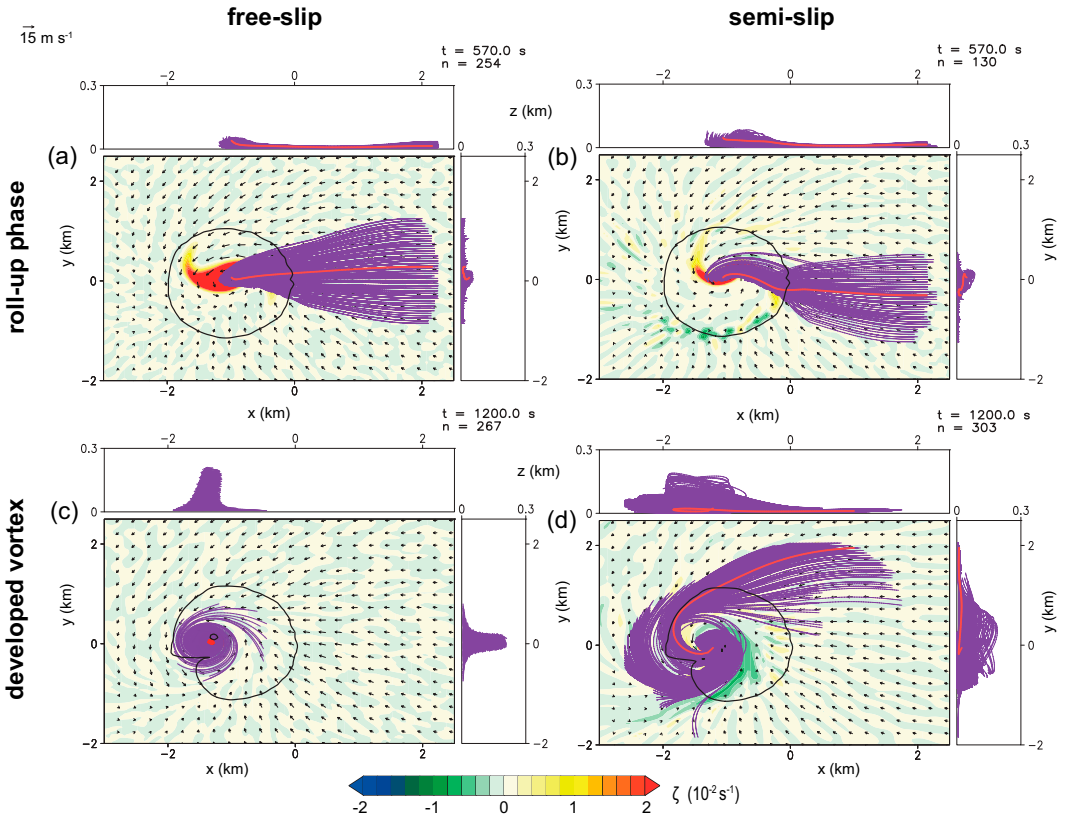

FIG. 9. (a),(b) Trajectories for the roll-up period at the time when the first symmetric vortex developed (reference time t_1 = 570 s). The parcels are the same as shown in Fig. 8. (c),(d) Trajectories for the developed vortex phase (reference time t_2 = 1200 s). In all figures, the vertical vorticity (shaded) and horizontal wind vectors are at the lowest model level and the 5 m s^{-1} updraft contour (black) is at 725 m. The red parcels are the average parcels for which budgets were calculated in Figs. 10 and 11. The total number of parcels is given in the top right of each plot, with only every tenth parcel shown in (c) for simplicity.

subtornadic vertical vorticity near the surface, which often takes the form of more or less elongated vortex patches. Axisymmetrization (Dahl 2020) and intensification of such a vortex patch below the updraft leads to a low-pressure core and, in simulations with surface drag, a corner-like flow (Davies-Jones 2015). With the formation of the corner-like flow, the parcels' horizontal vorticity may be tilted abruptly into the vertical practically at the surface. Therefore, the in-and-up mechanism begins to dominate the near-ground vorticity dynamics at this stage.

The proposed transition of mechanisms is consistent with the extant literature (Table 1). The downdraft mechanism has mainly been identified in studies that targeted the low-level mesocyclone or subtornadic vertical vorticity maxima near the surface. In contrast, the in-and-up mechanism has been found in studies analyzing the vertical vorticity source of TLVs, i.e., those vortices with tornadic values of vertical vorticity and hence likely some semblance of a corner flow. The simulations in the latter studies also tended to have a relatively high horizontal and vertical resolution, which is advantageous to resolve TLV structure and the rapid upward-turning of the flow near the ground. Last, most studies that showed the in-and-up mechanism used a semi-slip bottom boundary condition, which seems necessary to produce a well-pronounced corner-like flow in most cases, as will be discussed in section 4c.

It is noteworthy that the in-and-up mechanism in a mature vortex is different from the upward tilting of horizontal vorticity along a gust front, analyzed by Davies-Jones and Markowski (2013). In their scenario, there is a high-pressure perturbation with reduction of horizontal vorticity near the vertical velocity gradient. In contrast, the tornado has a low-pressure perturbation, which acts to increase horizontal vorticity via stretching. Furthermore, Markowski's (2016) results might at first appear contradicting the findings here. He showed that baroclinically enhanced circulation dominated for the times with the strongest tornado intensity. In contrast, herein horizontal vorticity that contributed to the in-and-up mechanism was mainly generated via surface drag and stretching. However, any horizontal vorticity can be tilted at the base of the vortex, suggesting that baroclinically generated horizontal vorticity can potentially play a role at this stage. The same argument also implies that environmental horizontal vorticity (Dahl et al. 2014; Dahl 2015) might be

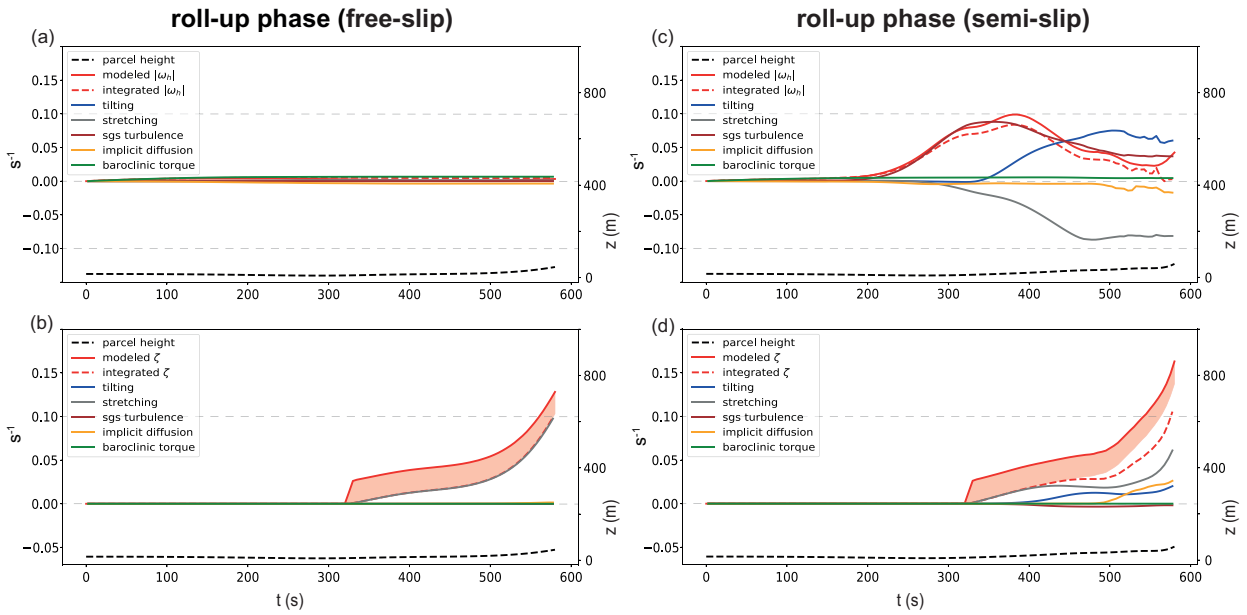

FIG. 10. Vorticity budgets for the red (average) parcels in Figs. 9a and 9b: (a),(c) horizontal vorticity and (b),(d) vertical vorticity. The parcel height is indicated on the secondary y axis (in m). The red shading illustrates the part of ζ that was added artificially via the vortex patch and hence resulted in a difference to the integrated ζ. This shaded $\Delta\zeta$ is constant at all times after 330 s, so any further difference between the modeled and integrated ζ is due to errors in integration.

an important source of vorticity for mature tornadoes, opening a possible pathway by which storm environments could directly influence vortex intensity. Ongoing research by the authors is investigating this possibility.

b. Rapid vortex intensification resulting from the transition

The transition from the downdraft to the in-and-up mechanism marks an important change in the near-ground tornado dynamics. This transition could be a reason for some of the observed characteristics of tornadogenesis. Fischer and Dahl (2020) found that nontornadic and tornadic pseudostorms were separated by a bifurcation region, in which minor differences between storms could determine whether tornadogenesis succeeded or not (note that these simulations were free-slip). A similar tipping point has been identified by Coffer and Parker (2018). A cause for such a bifurcation could be the changes in vortex dynamics shown in the present study. Stronger low-level updrafts and favorable cold pool characteristics (which are influenced by environmental properties such as storm relative helicity and low-level moisture) support stronger vortex patches (Fischer and Dahl 2020). Sufficient intensification during axisymmetrization of these patches could facilitate the development of the corner-like flow. In this case, the downdraft mechanism would suddenly be replaced by the in-and-up mechanism and direct tilting of horizontal vorticity. At that point, a number of vorticity sources become available (aside from horizontal baroclinically produced vorticity, there is vorticity due to surface drag and a copious amount of ambient vorticity). Consequently, vortex intensification would not rely on vertical vorticity from the downdraft mechanism anymore, which is limited by baroclinic horizontal vorticity production and reorientation (Dahl 2015). One could argue that the downdraft mechanism is in a sense quite inefficient because parcels tend to have a large vorticity

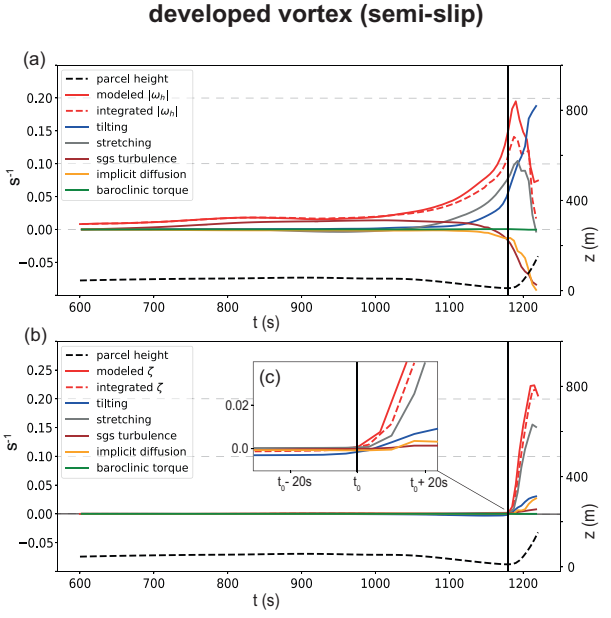

FIG. 11. Vorticity budgets as in Fig. 10, but for the developed tornado phase of the semi-slip run (average parcel in Fig. 9d). A zoomed-in view of the time period when the parcel entered the vortex is shown in (c) with the time on the x axis being relative to the time t_0 when the parcels reached the nadir. This time is marked with a vertical black line in all panels.

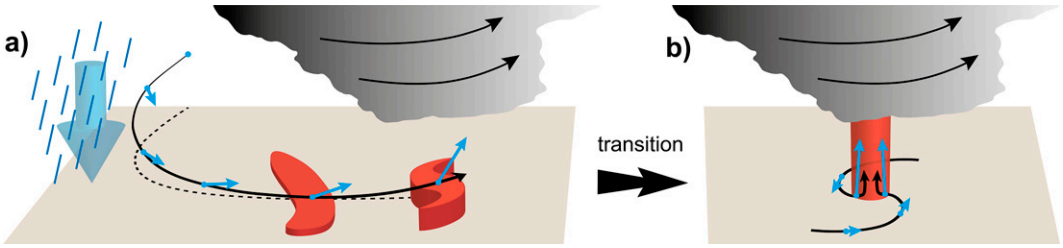

FIG. 12. Conceptual model of the transition of mechanisms during tornadogenesis. This model of tornadogenesis on the vortex scale can be seen as an extension of the final two steps of tornadogenesis on the storm scale as described in Davies-Jones (2015). (a) Evolution of the vorticity vector (blue) along a typical trajectory (solid black line; projection on the ground as a dashed line) experiencing the downdraft mechanism and entering a pretornadic vertical vorticity maximum (vortex patch) near the ground. This vortex patch then rolls up into a rather symmetric vortex and intensifies below the mesocyclone. (b) A developed tornado with flow entering the vortex near the ground, illustrated by streamlines (thick black) and vorticity vectors (blue). The horizontal vorticity is tilted abruptly into the vertical near the ground.

magnitude, but only a small vertical component can be utilized. Hence, the transition to the in-and-up mechanism could lead to a rather abrupt increase in swirl velocity and the often rapid formation of a visible condensation funnel.

c. *Sensitivity to the bottom-boundary condition*

In section 3, the simulation with a free-slip bottom boundary condition produced a vortex in near cyclostrophic balance, disabling the transition to the in-and-up mechanism. However, Rotunno et al. (2017) and Boyer and Dahl (2020), who also used a free-slip bottom boundary, seem to show the in-and-up mechanism for parcels entering their TLVs. In fact, for some variations of the experiment design of the idealized vortex patch simulations in section 3 (e.g., changing the grid spacing or the location of the patch), the resulting vortex did develop an endwall jet close to the ground for short time periods, even in the free-slip simulations. We decided not to analyze such a simulation in section 3 because the jet feature is likely not equivalent to the corner flow found in real tornadoes, but instead seemed to be a downward extension of the main updraft on one side of the vortex. Weak upward motion near the ground is common in idealized free-slip simulations (see e.g., Fiedler 2017), but it seems possible that intense free-slip vortices can also reproduce the in-and-up mechanism when vortex-external processes disrupt cyclostrophic balance. Since TLVs tend to be embedded in outflow air with much more unsteady flow, this could be a common behavior in full-physics simulations. Furthermore, the idealized simulations in section 3 lacked a mesocyclone, which could also have aided the in-and-up mechanism in Rotunno et al. (2017) and Boyer and Dahl (2020) to some degree. Still, including surface drag in the simulations seems necessary to reliably produce realistic near-ground vorticity dynamics.

5. Summary

Past supercell simulation studies have shown that the mechanisms responsible for large near-ground vertical vorticity associated with tornadoes broadly fall into two categories, the first one requiring a downdraft (here called downdraft mechanism) and the second one requiring only an updraft with abrupt upward tilting of large horizontal vorticity near the ground (referred to as the in-and-up mechanism). To clarify which mechanism is important in which situation, this study analyzed vertical vorticity maxima in both full-physics and highly idealized simulations. We specifically focused on the differences in vorticity dynamics of pretornadic vortex patches and mature tornado-like vortices. Parcels which descended below the lowest scalar model level were excluded and the trajectory analyses were largely based on average parcels to maximize the robustness of the results. These results suggest the following picture.

Vertical vorticity maxima in the supercell outflow are generated via the downdraft mechanism and organized in vortex patches (Fig. 12a). While being advected into an updraft region, these patches undergo an axisymmetrization and intensification dominated by vertical stretching (Fig. 12a). Near-ground horizontal vorticity plays a negligible role at this stage. The resulting rather symmetric vortex develops a low-pressure center while intensifying. In simulations with a semi-slip bottom boundary condition (and in real tornadoes), surface drag then allows for a force imbalance that results in radial inflow, giving rise to a swirling endwall jet and corner flow (or an annular corner flow around a central downdraft for two-celled vortices). At this stage, parcels entering the vortex in the spiraling inflow acquire vertical vorticity practically at the surface via rapid tilting of horizontal vorticity and subsequent stretching (Fig. 12b). Hence, the in-and-up mechanism becomes the dominant mechanism for maintaining large vertical vorticity near the ground. Several further aspects are noteworthy:

- Both mechanisms play vital roles during the tornado life cycle, which explains why they have both been found in the previous literature. Depending on the stage at which the vortex is analyzed, either the downdraft or the in-and-up mechanism is more important.

- The downdraft mechanism (and likely baroclinic horizontal vorticity generation) is needed to start the process. Subsequently, the in-and-up mechanism can tilt any available horizontal vorticity into the vertical directly. Therefore, the transition between the mechanisms during tornadogenesis could potentially lead to a rapid increase in tornado intensity.
- In the vicinity of the simulated tornadoes, surface drag and horizontal stretching were the main contributors to large horizontal vorticity, available to be tilted into the vertical via the in-and-up mechanism. However, baroclinically generated, and importantly, even environmental horizontal vorticity could contribute in the same way and could therefore influence the dynamics of mature tornadoes.
- Some parcels may very well also have some vertical vorticity as they enter the mature vortex. However, positive vertical vorticity (produced during descent) seems no longer necessary for tornado maintenance.

Acknowledgments. This research was supported by NSF Grant AGS-1651786. We thank Drs. Brice Coffer and Matt Parker for their advice regarding the full-physics simulations and Dr. George Bryan for his ongoing support of CM1. The three anonymous reviewers offered many helpful suggestions for improvement. We also acknowledge Drs. Paul Markowski, Matt Parker, Chris Weiss, and Eric Bruning for numerous insightful discussions.

Data availability statement. The CM1 source code and namelist files are included as online supplemental material. Additional material is available from the corresponding author upon request.

REFERENCES

Adlerman, E., K. Droegemeier, and R. Davies-Jones, 1999: A numerical simulation of cyclic mesocyclogenesis. *J. Atmos. Sci.*, **56**, 2045–2069, https://doi.org/10.1175/1520-0469(1999)056<2045:ANSOCM>2.0.CO;2.

Boyer, C. H., and J. M. Dahl, 2020: The mechanisms responsible for large near-surface vertical vorticity within simulated supercells and quasi-linear storms. *Mon. Wea. Rev.*, **148**, 4281–4297, https://doi.org/10.1175/MWR-D-20-0082.1.

Bryan, G. H., and J. M. Fritsch, 2002: A benchmark simulation for moist nonhydrostatic numerical models. *Mon. Wea. Rev.*, **130**, 2917–2928, https://doi.org/10.1175/1520-0493(2002)130<2917:ABSFMN>2.0.CO;2.

——, N. A. Dahl, D. S. Nolan, and R. Rotunno, 2017: An eddy injection method for large-eddy simulations of tornado-like vortices. *Mon. Wea. Rev.*, **145**, 1937–1961, https://doi.org/10.1175/MWR-D-16-0339.1.

Coffer, B. E., and M. D. Parker, 2017: Simulated supercells in nontornadic and tornadic VORTEX2 environments. *Mon. Wea. Rev.*, **145**, 149–180, https://doi.org/10.1175/MWR-D-16-0226.1.

——, and ——, 2018: Is there a "tipping point" between simulated nontornadic and tornadic supercells in VORTEX2 environments? *Mon. Wea. Rev.*, **146**, 2667–2693, https://doi.org/10.1175/MWR-D-18-0050.1.

——, ——, J. M. Dahl, L. J. Wicker, and A. J. Clark, 2017: Volatility of tornadogenesis: An ensemble of simulated nontornadic and tornadic supercells in VORTEX2 environments. *Mon. Wea. Rev.*, **145**, 4605–4625, https://doi.org/10.1175/MWR-D-17-0152.1.

Coniglio, M. C., and M. D. Parker, 2020: Insights into supercells and their environments from three decades of targeted radiosonde observations. *Mon. Wea. Rev.*, **148**, 4893–4915, https://doi.org/10.1175/MWR-D-20-0105.1.

Dahl, J. M. L., 2015: Near-ground rotation in simulated supercells: On the robustness of the baroclinic mechanism. *Mon. Wea. Rev.*, **143**, 4929–4942, https://doi.org/10.1175/MWR-D-15-0115.1.

——, 2017: Tilting of horizontal shear vorticity and the development of updraft rotation in supercell thunderstorms. *J. Atmos. Sci.*, **74**, 2997–3020, https://doi.org/10.1175/JAS-D-17-0091.1.

——, 2020: Near-surface vortex formation in supercells from the perspective of vortex patch dynamics. *Mon. Wea. Rev.*, **148**, 3533–3547, https://doi.org/10.1175/MWR-D-20-0080.1.

——, 2021: Centrifugal waves in tornado-like vortices: Kelvin's solutions and their applications to multiple-vortex development and vortex breakdown. *Mon. Wea. Rev.*, **149**, 3173–3216, https://doi.org/10.1175/MWR-D-20-0426.1.

——, M. D. Parker, and L. J. Wicker, 2014: Imported and storm-generated near-ground vertical vorticity in a simulated supercell. *J. Atmos. Sci.*, **71**, 3027–3051, https://doi.org/10.1175/JAS-D-13-0123.1.

Davies-Jones, R., 1984: Streamwise vorticity: The origin of updraft rotation in supercell storms. *J. Atmos. Sci.*, **41**, 2991–3006, https://doi.org/10.1175/1520-0469(1984)041<2991:SVTOOU>2.0.CO;2.

——, 2002: Linear and nonlinear propagation of supercell storms. *J. Atmos. Sci.*, **59**, 3178–3205, https://doi.org/10.1175/1520-0469(2003)059<3178:LANPOS>2.0.CO;2.

——, 2015: A review of supercell and tornado dynamics. *Atmos. Res.*, **158–159**, 274–291, https://doi.org/10.1016/j.atmosres.2014.04.007.

——, 2021: Invented forces in supercell models. *J. Atmos. Sci.*, **78**, 2927–2939, https://doi.org/10.1175/JAS-D-21-0082.1.

——, and H. Brooks, 1993: Mesocyclogenesis from a theoretical perspective. *The Tornado: Its Structure, Dynamics, Prediction, and Hazards, Geophys. Monogr.*, Vol. 79, Amer. Geophys. Union, 105–114.

——, and P. Markowski, 2013: Lifting of ambient air by density currents in sheared environments. *J. Atmos. Sci.*, **70**, 1204–1215, https://doi.org/10.1175/JAS-D-12-0149.1.

Davies-Jones, R. P., 1982: Observational and theoretical aspects of tornadogenesis. *Intense Atmospheric Vortices*, L. Bengtsson and J. Lighthill, Eds., Springer, 175–189.

Fiedler, B. H., 1993: Numerical simulation of axisymmetric tornadogenesis in forced convection. *The Tornado: Its Structure, Dynamics, Prediction, and Hazards, Geophys. Monogr.*, Vol. 79, Amer. Geophys. Union, 41–48.

——, 2017: Axisymmetric tornado simulations with a semi-slip boundary. *Fluids*, **2**, 68, https://doi.org/10.3390/fluids2040068.

——, and R. Rotunno, 1986: A theory for the maximum wind speeds in tornado-like vortices. *J. Atmos. Sci.*, **43**, 2328–2340, https://doi.org/10.1175/1520-0469(1986)043<2328:ATOTMW>2.0.CO;2.

Fischer, J., and J. M. L. Dahl, 2020: The relative importance of updraft and cold pool characteristics in supercell

tornadogenesis using highly idealized simulations. *J. Atmos. Sci.*, **77**, 4089–4107, https://doi.org/10.1175/JAS-D-20-0126.1.

Flournoy, M. D., and M. C. Coniglio, 2019: Origins of vorticity in a simulated tornadic mesovortex observed during PECAN on 6 July 2015. *Mon. Wea. Rev.*, **147**, 107–134, https://doi.org/10.1175/MWR-D-18-0221.1.

French, M. M., H. B. Bluestein, I. Popstefanija, C. A. Baldi, and R. T. Bluth, 2013: Reexamining the vertical development of tornadic vortex signatures in supercells. *Mon. Wea. Rev.*, **141**, 4576–4601, https://doi.org/10.1175/MWR-D-12-00315.1.

Klemp, J. B., and R. Rotunno, 1983: A study of the tornadic region within a supercell thunderstorm. *J. Atmos. Sci.*, **40**, 359–377, https://doi.org/10.1175/1520-0469(1983)040<0359:ASOTTR>2.0.CO;2.

Lewellen, D. C., and W. S. Lewellen, 2007: Near-surface intensification of tornado vortices. *J. Atmos. Sci.*, **64**, 2176–2194, https://doi.org/10.1175/JAS3965.1.

Lewellen, W. S., 1993: Tornado vortex theory. *The Tornado: Its Structure, Dynamics, Prediction, and Hazards, Geophys. Monogr.*, Vol. 79, Amer. Geophys. Union, 19–39.

Ludlam, F. H., 1963: Severe local storms: A review. *Severe Local Storms, Meteor. Monogr.*, No. 5, Amer. Meteor. Soc., 1–32, https://doi.org/10.1007/978-1-940033-56-3_1.

Markowski, P. M., 2016: An idealized numerical simulation investigation of the effects of surface drag on the development of near-surface vertical vorticity in supercell thunderstorms. *J. Atmos. Sci.*, **73**, 4349–4385, https://doi.org/10.1175/JAS-D-16-0150.1.

——, and Y. P. Richardson, 2014: The influence of environmental low-level shear and cold pools on tornadogenesis: Insights from idealized simulations. *J. Atmos. Sci.*, **71**, 243–275, https://doi.org/10.1175/JAS-D-13-0159.1.

——, and G. H. Bryan, 2016: LES of laminar flow in the PBL: A potential problem for convective storm simulations. *Mon. Wea. Rev.*, **144**, 1841–1850, https://doi.org/10.1175/MWR-D-15-0439.1.

——, Y. Richardson, and G. Bryan, 2014: The origins of vortex sheets in a simulated supercell thunderstorm. *Mon. Wea. Rev.*, **142**, 3944–3954, https://doi.org/10.1175/MWR-D-14-00162.1.

——, N. T. Lis, D. D. Turner, T. R. Lee, and M. S. Buban, 2019: Observations of near-surface vertical wind profiles and vertical momentum fluxes from VORTEX-SE 2017: Comparisons to Monin–Obukhov similarity theory. *Mon. Wea. Rev.*, **147**, 3811–3824, https://doi.org/10.1175/MWR-D-19-0091.1.

Mashiko, W., 2016: A numerical study of the 6 May 2012 Tsukuba City supercell tornado. Part II: Mechanisms of tornadogenesis. *Mon. Wea. Rev.*, **144**, 3077–3098, https://doi.org/10.1175/MWR-D-15-0122.1.

——, H. Niino, and T. Kato, 2009: Numerical simulation of tornadogenesis in an outer-rainband minisupercell of Typhoon Shanshan on 17 September 2006. *Mon. Wea. Rev.*, **137**, 4238–4260, https://doi.org/10.1175/2009MWR2959.1.

Naylor, J., and M. S. Gilmore, 2012: Convective initiation in an idealized cloud model using an updraft nudging technique. *Mon. Wea. Rev.*, **140**, 3699–3705, https://doi.org/10.1175/MWR-D-12-00163.1.

——, and ——, 2014: Vorticity evolution leading to tornadogenesis and tornadogenesis failure in simulated supercells. *J. Atmos. Sci.*, **71**, 1201–1217, https://doi.org/10.1175/JAS-D-13-0219.1.

Nolan, D. S., 2012: Three-dimensional instabilities in tornado-like vortices with secondary circulations. *J. Fluid Mech.*, **711**, 61–100, https://doi.org/10.1017/jfm.2012.369.

Orf, L., R. Wilhelmson, B. Lee, C. Finley, and A. Houston, 2017: Evolution of a long-track violent tornado within a simulated supercell. *Bull. Amer. Meteor. Soc.*, **98**, 45–68, https://doi.org/10.1175/BAMS-D-15-00073.1.

Parker, M. D., 2012: Impacts of lapse rates on low-level rotation in idealized storms. *J. Atmos. Sci.*, **69**, 538–559, https://doi.org/10.1175/JAS-D-11-058.1.

——, 2014: Composite VORTEX2 supercell environments from near-storm soundings. *Mon. Wea. Rev.*, **142**, 508–529, https://doi.org/10.1175/MWR-D-13-00167.1.

——, and J. M. L. Dahl, 2015: Production of near-surface vertical vorticity by idealized downdrafts. *Mon. Wea. Rev.*, **143**, 2795–2816, https://doi.org/10.1175/MWR-D-14-00310.1.

Rasmussen, E. N., and D. O. Blanchard, 1998: A baseline climatology of sounding-derived supercell and tornado forecast parameters. *Wea. Forecasting*, **13**, 1148–1164, https://doi.org/10.1175/1520-0434(1998)013<1148:ABCOSD>2.0.CO;2.

Roberts, B., M. Xue, A. D. Schenkman, and D. T. Dawson, 2016: The role of surface drag in tornadogenesis within an idealized supercell simulation. *J. Atmos. Sci.*, **73**, 3371–3395, https://doi.org/10.1175/JAS-D-15-0332.1.

——, ——, and D. T. Dawson, 2020: The effect of surface drag strength on mesocyclone intensification and tornadogenesis in idealized supercell simulations. *J. Atmos. Sci.*, **77**, 1699–1721, https://doi.org/10.1175/JAS-D-19-0109.1.

Rotunno, R., 1981: On the evolution of thunderstorm rotation. *Mon. Wea. Rev.*, **109**, 577–586, https://doi.org/10.1175/1520-0493(1981)109<0577:OTEOTR>2.0.CO;2.

——, 2013: The fluid dynamics of tornadoes. *Annu. Rev. Fluid Mech.*, **45**, 59–84, https://doi.org/10.1146/annurev-fluid-011212-140639.

——, and J. B. Klemp, 1982: The influence of the shear-induced pressure gradient on thunderstorm motion. *Mon. Wea. Rev.*, **110**, 136–151, https://doi.org/10.1175/1520-0493(1982)110<0136:TIOTSI>2.0.CO;2.

——, and ——, 1985: On the rotation and propagation of simulated supercell thunderstorms. *J. Atmos. Sci.*, **42**, 271–292, https://doi.org/10.1175/1520-0469(1985)042<0271:OTRAPO>2.0.CO;2.

——, P. M. Markowski, and G. H. Bryan, 2017: "Near ground" vertical vorticity in supercell thunderstorm models. *J. Atmos. Sci.*, **74**, 1757–1766, https://doi.org/10.1175/JAS-D-16-0288.1.

Schenkman, A. D., and M. Xue, 2016: Bow-echo mesovortices: A review. *Atmos. Res.*, **170**, 1–13, https://doi.org/10.1016/j.atmosres.2015.11.003.

——, ——, and M. Hu, 2014: Tornadogenesis in a high-resolution simulation of the 8 May 2003 Oklahoma City supercell. *J. Atmos. Sci.*, **71**, 130–154, https://doi.org/10.1175/JAS-D-13-073.1.

Simpson, M. W., and A. Glezer, 2016: Buoyancy-induced, columnar vortices. *J. Fluid Mech.*, **804**, 712–748, https://doi.org/10.1017/jfm.2016.541.

Tao, T., and T. Tamura, 2020: Numerical study of the 6 May 2012 Tsukuba supercell tornado: Vorticity sources responsible for tornadogenesis. *Mon. Wea. Rev.*, **148**, 1205–1228, https://doi.org/10.1175/MWR-D-19-0095.1.

Trapp, R. J., and M. L. Weisman, 2003: Low-level mesovortices within squall lines and bow echoes. Part II: Their genesis and implications. *Mon. Wea. Rev.*, **131**, 2804–2823, https://doi.org/10.1175/1520-0493(2003)131<2804:LMWSLA>2.0.CO;2.

Vande Guchte, A., and J. M. L. Dahl, 2018: Sensitivities of parcel trajectories beneath the lowest scalar model level of a Lorenz vertical grid. *Mon. Wea. Rev.*, **146**, 1427–1435, https://doi.org/10.1175/MWR-D-17-0190.1.

Wicker, L. J., and R. B. Wilhelmson, 1993: Numerical simulation of tornadogenesis within a supercell thunderstorm. *The Tornado: Its Structure, Dynamics, Prediction, and Hazards, Geophys. Monogr.*, Vol. 79, Amer. Geophys. Union, 75–88.

——, and ——, 1995: Simulation and analysis of tornado development and decay within a three-dimensional supercell thunderstorm. *J. Atmos. Sci.*, **52**, 2675–2703, https://doi.org/10.1175/1520-0469(1995)052<2675:SAAOTD>2.0.CO;2.

Yokota, S., H. Niino, H. Seko, M. Kunii, and H. Yamauchi, 2018: Important factors for tornadogenesis as revealed by high-resolution ensemble forecasts of the Tsukuba supercell tornado of 6 May 2012 in Japan. *Mon. Wea. Rev.*, **146**, 1109–1132, https://doi.org/10.1175/MWR-D-17-0254.1.